ADVANCED MATERIALS TECHNOLOGIES
www.advmattechnol.de

Multi-Photon 4D Printing of Complex Liquid Crystalline Microstructures by In Situ Alignment Using Electric Fields

Alexander Münchinger, Vincent Hahn, Dominik Beutel, Simon Woska, Joël Monti, Carsten Rockstuhl, Eva Blasco, and Martin Wegener**

An approach is presented to align the direction of liquid crystal networks or elastomers in situ during multi-photon laser printing for each voxel in three dimensions by applying a quasi-static electric field with variable orientation. This approach enables the making of 3D micro-heterostructures operating under ambient conditions that show large-amplitude elastic actuation, with temperature serving as the stimulus ("4D microstructures"). The approach involves two novelties. First, a dedicated sample cell with a variable height suitable for laser printing is introduced. It is based on optically transparent electrodes and allows to apply arbitrary electric field vectors in three dimensions, for example, parallel or normal to the substrate plane. Second, a variable optical phase plate combined with a pivotable half-wave plate warrants a single well-defined laser focus for nearly all possible quasi-static electric field vectors. Without the latter, one generally obtains two spatially separated laser foci, an ordinary and an extraordinary one, due to the optical birefringence of the medium induced by the alignment of the liquid crystal director via the applied quasi-static electric field. The versatility of the approach is illustrated by manufacturing and characterizing several exemplary architectures.

A. Münchinger, V. Hahn, S. Woska, M. Wegener
Institute of Applied Physics (APH)
Karlsruhe Institute of Technology (KIT)
76131 Karlsruhe, Germany
E-mail: alexander.muenchinger@kit.edu; martin.wegener@kit.edu

V. Hahn, J. Monti, C. Rockstuhl, E. Blasco, M. Wegener
Institute of Nanotechnology (INT)
Karlsruhe Institute of Technology (KIT)
76344 Eggenstein-Leopoldshafen, Germany

D. Beutel, C. Rockstuhl
Institute of Theoretical Solid State Physics
Karlsruhe Institute of Technology (KIT)
76131 Karlsruhe, Germany

E. Blasco
Institute of Organic Chemistry
Heidelberg University
69120 Heidelberg, Germany

E. Blasco
Centre for Advanced Materials
Heidelberg University
69120 Heidelberg, Germany

The ORCID identification number(s) for the author(s) of this article can be found under https://doi.org/10.1002/admt.202100944.

DOI: 10.1002/admt.202100944

1. Introduction

Additive manufacturing of stimulus-responsive 3D microstructures, also referred to as 4D printing, is a frontier of materials research[1–5] with numerous potential applications in soft micro-robotics,[6–11] time-dependent (space-time) metamaterials,[12,13] optics,[14–17] and generally in active micro- and nano-structures.[18–22] In particular, repeatable large-amplitude actuation is desirable in response to conveniently accessible external stimuli such as temperature,[15–20,23] light intensity,[7,8,11,19,21] pH value,[18,20,24,25] magnetic fields,[9–11] etc. For many applications in the life sciences and in micro-fluidics, operation under aqueous conditions is desirable. There, based on hydrogels, complex architectures exhibiting large-amplitude repeatable actuation via small temperature swings or light illumination have been achieved by several groups.[18–20,23] In the technical sciences, on the other hand, operation under ambient conditions is required. Hydrogels dehydrate under ambient conditions, thus lose their responsiveness and are hence not an option. Among the various functioning stimulus-responsive material systems that have been introduced for ambient operation,[17,26–29] liquid crystal networks (LCN) or elastomers appear as a particularly attractive option (also see the reviews[4,30–33]). Actuatable micro-grippers,[7] micro-walkers,[8] tunable optical micro-resonators[14,15] and other responsive microstructures[34] have been realized by using commercially available multi-photon 3D laser printing machine tools.

The actuation of LCNs is based on a phase transition, which brings the system from a low-temperature low-entropy phase, in which the individual liquid crystal molecules are aligned with respect to each other, to a high-temperature high-entropy phase in which the molecules are randomly oriented. Obviously, this transition requires the alignment of the liquid crystal molecules (hence of the director) before or during polymerization.

Outside of multi-photon 3D printing of liquid crystal-based inks, the director alignment in a thin layer on a substrate surface has been accomplished by exploiting the polarization of light.[35–38] The director orientation in this thin layer is then transferred to the liquid crystal molecules on top. Other authors have microstructured a polymer layer on the substrate surface

by either subtractive[39,40] or additive approaches.[41,42] Again, this pre-structuring aligns the director of the LCNs in contact with the surface. Additionally, mechanical alignment of the oligomer director has also been employed during 3D printing, for example, via the nozzle in a direct-ink-printing process.[43–50]

For multi-photon 3D laser printing, which enables finer features and which we use in this paper, alignment of the director has been accomplished by the close proximity of the molecules to properly prepared surfaces. This preparation was done, for example, by application and rubbing of a polyimide layer[7,8,14,51] or by surface functionalization with silanes.[15] By using planar pre-structuring of surfaces, the liquid crystal director field was even shaped into complex 2D patterns.[41,42] However, the involvement of surfaces does not allow to independently define the director at each point in 3D space, which is mandatory for complex architectures.

Herein, we introduce a novel approach that allows us to align the local liquid crystal director independently for each volume element (voxel) in 3D space by applying a quasi-static electric field with variable field direction in situ during the multi-photon 3D laser printing process. Upon photo-polymerization, the instantaneous director orientation is fixed in the printed voxel, and a different electric-field vector can be applied for the next voxel. The underlying setup is based on multi-photon 3D laser microprinting in a dedicated sample cell containing a set of optically transparent electrodes. The setup also comprises an adjustable optical phase plate combined with a pivotable half-wave plate. This combination allows us to obtain a single well-defined laser focus despite focusing into an optically strongly birefringent medium, which generally leads to two spatially separated laser foci, an ordinary and an extraordinary one. We illustrate the potential of the approach by manufacturing and characterizing several exemplary architectures.

2. Results

In the following, we present our strategy to align the director of a liquid crystalline (LC) ink during multi-photon 3D laser printing via electric fields to obtain LCN structures with a spatially varying director. Afterward, we discuss how to focus the printing laser inside the birefringent LC ink without major distortions of the focus. Finally, we show examples of complex 3D microstructures exhibiting different spatial distributions of the director orientation to prove the capabilities of our approach.

2.1. Director Alignment Strategy

To induce the quasi-static electric fields that align the director during printing, a structured electrode is incorporated above the objective lens of a 3D laser microprinting setup, as indicated in **Figure 1**a. The electrode is carried by a holder located around the objective lens that allows for a fine adjustment of the position and the orientation of the electrode. The electrode consists of an ordinary coverslip with structured indium tin oxide (ITO) patterns on the front and backside. The optically transparent ITO patterns are depicted schematically in Figure 1d. A reflection microscope image is shown in the inset of Figure 1a. In the microscope image, the front and the backside patterns appear in different interference colors. The more extensive pattern facing toward the objective lens appears blue, while the pattern on the opposite side appears green. The structured electrode is faced by a parallel ITO-coated substrate, which acts as the counter electrode.

In between the substrate and the electrode, an LC ink is applied. The ink used here has been reported elsewhere[15] and is further discussed in the Supporting Information. It exhibits a nematic mesophase and is liquid at room temperature. The ink contains the liquid crystal mixture E7. This mixture dissolves ordinary reactive mesogens[7,8,14–16,41,42,52] such that the ink is in the nematic phase at room temperature. Furthermore, E7 helps to lower the electric field strength at which the Fréedericksz transition occurs.

The printing process is schematically depicted in Figure 1b,c. In a first step, we might want to print a part of a structure with a horizontal director and therefore apply a horizontal electric field as shown in Figure 1b. The field aligns the reactive mesogens horizontally. Next, we fix the horizontal alignment into a voxel by a two-photon induced polymerization at the focus of a femtosecond pulsed laser.[51] By scanning the laser beam with galvanometer mirrors, it is possible to print voxels at different positions in a plane parallel to the substrate. We can print voxels at different distances from the substrate by moving the substrate away from the objective lens. Thereby, we can print a 3D structure with a horizontal director voxel by voxel. To print a following part of the structure with a vertical director, we apply a vertical electric field and repeat the process, as illustrated in Figure 1c. After the printing, we take the substrate with the printed structure attached to it and wash away the insufficiently polymerized liquid ink to obtain a 3D structure with a spatially varying director. This overall process requires that we are able to induce homogeneous electric fields within the region where the polymerization happens. This region is called the printing area and is marked in red in Figure 1d.

As a next step, we proved that the electrode system is able to induce sufficiently homogeneous electric fields along the coordinate axis shown in Figure 1d within the printing area. Therefore, we employed a finite element approach to solve the Poisson equation for the geometry depicted in Figure 1d. We applied two different sets of potentials V_i^x and V_i^z with $i = 1...6$ to the electrode pads for different distances h between the electrode and the substrate. Thereby, the superscript always labels the intended average direction of the field vector.

$$V_1^x = V_2^x = V_5^x = V_6^x = U^x, V_3^x = 0 \text{ V}, V_4^x = 2U^x \text{ with } U^x = 1428.6 \text{ V} \quad (1)$$

$$V_1^z = V_2^z = V_3^z = V_4^z = U^z, V_5^z = 0 \text{ V}, V_6^z = 3U^z \text{ with } U^z = 504.4 \text{ V} \quad (2)$$

The distance of the substrate and the electrode ranges from the initial height of 100 µm up to 1 mm.

As a result, we obtained the electric field distribution within the printing area. As desired, the fields point toward the x- and z-direction on average. The average magnitude is plotted in Figure 1e. To assess the homogeneity of the field regarding its magnitude, we calculated the modulus of the deviation of

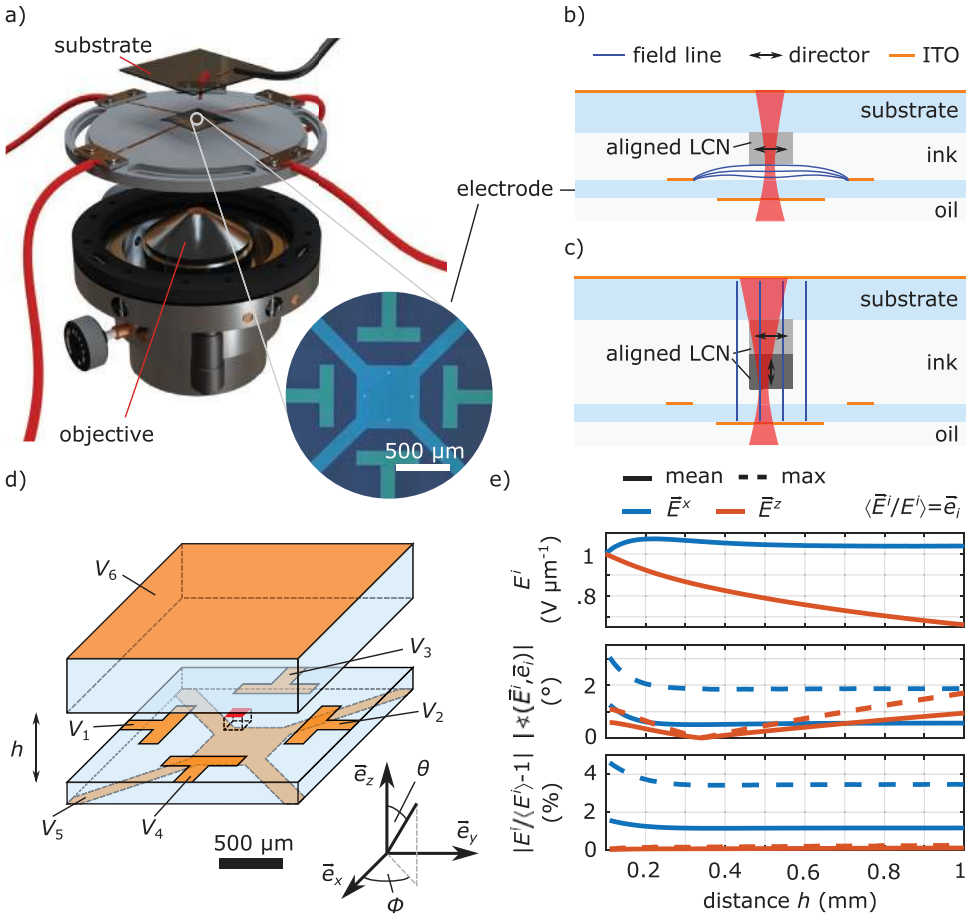

Figure 1. a) Sample cell including the objective lens inside the electrode holder, the electrode, and the substrate. The inset shows a microscope image of the patterned ITO electrode in a reflection illumination, causing different interference colors for the front and back pattern. b) A laser (red) is focused into the LC ink located between the electrode and the substrate. In parallel, the electrode induces a horizontal electric field to align the director of the ink. A two-photon absorption polymerization starts at the laser focus and fixes the horizontally pointing director of the forming LCN. c) A vertical field is applied and the LCN with a vertical director is printed. d) 3D schematic of the sample cell representing the geometry used for finite element simulations to calculate the electric fields for different heights h of the substrate. The electrical potentials applied to the electrode pads shown in orange are named V_j. The area marked in red represents the printing area located 100 µm above the electrode. e) Simulation results for the electric fields $\vec{E}^x$,$\vec{E}^z$ within the printing area for two different sets of potentials V_j^x, V_j^z. On average, $\vec{E}^x$ points in the x-direction and $\vec{E}^z$ in the z-direction. Symbols without accented arrow denote the modulus of the corresponding field. Solid lines represent the average over the printing area and dashed lines represent the maximum. The top panel shows the modulus of the fields for different heights of the substrate. The panels below quantify deviations from a homogeneous behavior. First, the modulus of the angle between the field and its mean direction is shown. Second the deviation of the modulus of the field from its mean modulus is plotted.

the magnitude to the mean magnitude within the printing area. Figure 1e shows the mean and the maximum within the printing area. The spatial distribution of this deviation is plotted in Figure S3, Supporting Information. Furthermore, we calculated the norm of the angle between the field direction and the desired field direction to assess the homogeneity concerning the targeted direction of the field. The mean and the maximum of this quantity within the printing area are presented in Figure 1e. The spatial distribution is plotted in Figure S3, Supporting Information. The angle deviation is below 1.5° in average and below 3° in maximum for heights below 1 mm. The deviation in magnitude is below 2% in average and below 4.6% in maximum for all heights below 1 mm. Therefore, we consider the fields for both configurations to be sufficiently homogeneous fields along the x- and z-direction. Due to the symmetry of the geometry, the same considerations hold for fields in the y-direction. The potentials to apply are

$$V_3^y = V_4^y = V_5^y = V_6^y = U^x,\ V_1^y = 0\ \text{V},\ V_2^y = 2U^x \tag{3}$$

However, we emphasize that not only fields along the principal axes can be generated. By superposition of these fields, the electrode system can induce homogeneous electric fields in any direction within the printing area. In spherical coordinates, we obtain Equation (4) for the potentials to apply to induce a field with strength E in direction (ϕ,θ) for a certain height h of the substrate.

$$V_i(E,\phi,\theta,h) = \frac{E}{E^x(h)}\left[\cos\phi\sin\theta V_i^x + \sin\phi\sin\theta V_i^y\right] + \frac{E}{E^z(h)}\cos\theta V_i^z + V_0, i = 1,\ldots,6 \tag{4}$$

A constant potential V_0 can be added to shift the potentials to reasonable values. In our setup, we do not apply a strictly static

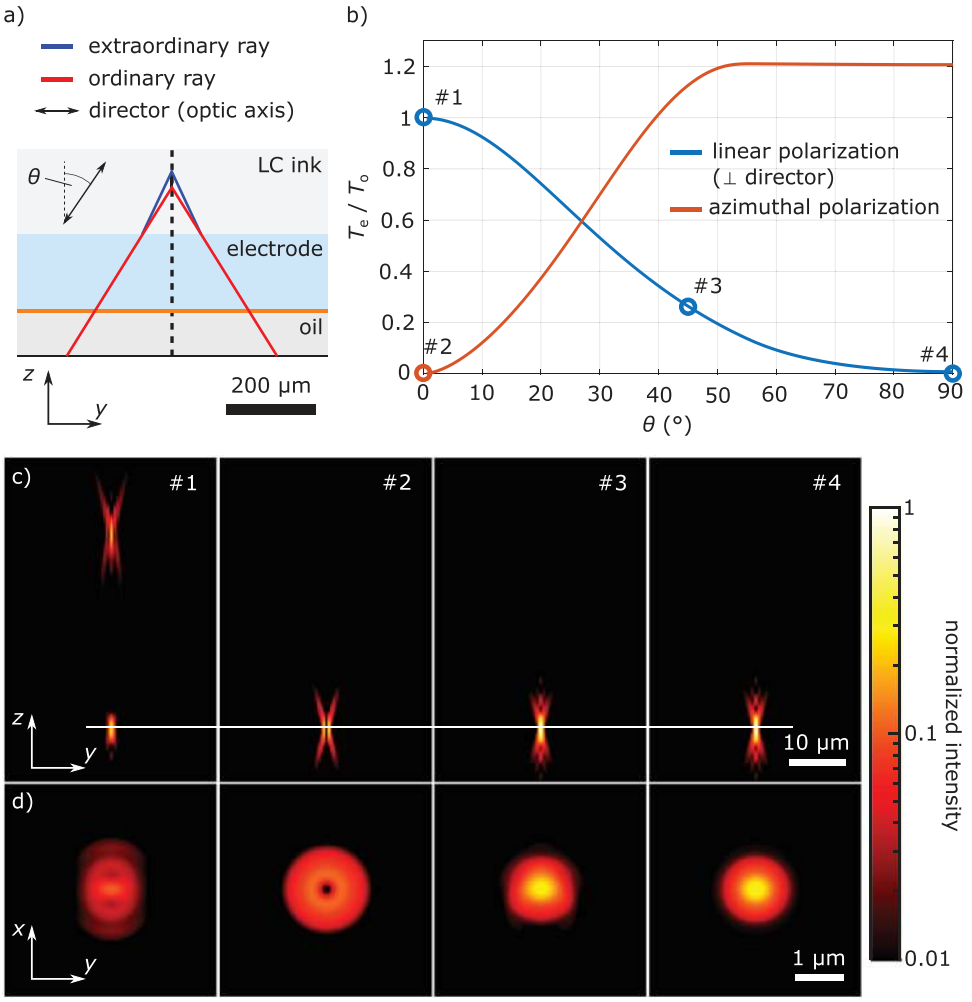

Figure 2. a) A schematic cut through the center of the sample cell showing two rays of the focused laser. In ray optics, at the interface of the electrode and the ink, the light is refracted into an ordinary and an extraordinary ray. The direction and the intensity of the refracted rays depend on the optic axis of the LC ink that coincides with its director. b) The power of the laser beam transmitted into the extraordinary focus divided by the power transmitted into the ordinary focus for all possible director angles θ with respect to the optical axis. The red curve represents an azimuthally polarized laser and the blue curve a laser polarized linearly and perpendicular to the director. Four different cases are highlighted. c,d) Full-wave calculations. c) The normalized intensity distribution inside the ink in the *y*-*z* plane for the highlighted cases. Case #1 shows a combination of polarization and director that leads to two foci. Only a single focus is visible for case #2, #3 and #4. d) The normalized intensity in the *x*-*y* plane cutting the foci as indicated by the white line in panel (c).

electric field but a sinusoidal quasi-static electric field with a frequency of 800 Hz to increase the breakdown voltage.[53] We adjust the potentials via six variable voltage dividers built from variable turning plate capacitors connected to an amplifier capable of output signals with an amplitude of 3 kV.

This setup allows us to align the director of the LC ink in any direction, which is necessary to print LCN with a certain director. However, it is also necessary to focus the printing laser in a single confined spot within the printing area. This task is non-trivial because the LC ink is a uniaxial, strongly birefringent optical medium with its optic axis parallel to the director.

2.2. Focusing into Birefringent Media

For our considerations, we assume the ordinary refractive index of the LC ink and the refractive indices of the electrode and the immersion oil to be the same. This means that a wave that hits the interface of the electrode and the LC ink induces an ordinary wave, which is not refracted. More generally, an extraordinary wave is induced as well. This partial wave is refracted into a different direction. This situation is schematically depicted in **Figure 2**a. A suppression of the extraordinary wave, for example by a suitable polarization of the laser, must automatically lead to a confined laser focus, since then the problem is equivalent to focusing into an ordinary medium with a single refractive index for which the objective lens is optimized.

In the following, we show that the extraordinary waves can be completely suppressed for a horizontal and a vertical director by choosing a linear polarization perpendicular to the director or an azimuthal polarization, respectively. To prove that, we first discuss the ratio of the power transmitted into the

extraordinary waves and the ordinary waves. Afterward, we will present the normalized intensity distribution in the ink.

To compute the power transmitted into the ordinary and extraordinary waves, respectively, we calculated the Fourier spectrum of the refracted field via the Richards-Wolf method.[54] For every plane wave in the spectrum, we calculated the corresponding Poynting vectors of the refracted ordinary and extraordinary wave in the LC ink via the Fresnel equations for the birefringent case.[55] Thereby, we obtained coefficients for the fraction of the power transmitted for every plane wave in the spectrum into the ordinary and the extraordinary waves, respectively. By integrating over the transmitted power of every plane wave, we obtained the overall power of the printing laser transmitted into the ordinary and the extraordinary waves.

Figure 2b shows the power transmitted into extraordinary waves divided by the power transmitted into the ordinary waves for an azimuthal and a linear polarization perpendicular to the director. It is plotted for all possible configurations of the director. For a director perpendicular to the interface ($\theta = 0°$), the fraction is zero for an azimuthal polarization. For a director parallel to the interface ($\theta = 90°$), it is zero for linear polarization perpendicular to the director. The fraction is below 0.5 for angles of $\theta > 35°$ for linear polarization. For angles of $\theta < 25°$ it is smaller than 0.5 for azimuthal polarization. We conclude that we obtain a single confined laser focus for a vertical director in the case of azimuthal polarization and for a horizontal director in the case of linear polarization perpendicular to the director. The calculations also raise hopes that it is possible to print intermediate director configurations, for which the transmission into the ordinary mode is much larger than into the extraordinary mode.

To put these findings onto a more solid foundation, we calculated the intensity distribution inside the LC ink by propagating the refracted field calculated by the Richards-Wolf method. The exact procedure has been described elsewhere.[15,56] Figure 2c shows the normalized intensity in the plane of the director for four different configurations of director and polarization. Figure 2d shows the corresponding normalized intensity in the printing area. In the first configuration, a linear polarized laser is focused inside the LC ink with a vertical director. In this configuration, two foci appear on top of each other along the optical axis. By changing to azimuthal polarization, which is depicted in configuration two, the extraordinary focus vanishes. The remaining focus has a toroidal shape in the focal plane. In configurations three and four, the polarization is linear, while θ equals 45° and 90°. For both configurations, a confined single laser focus appears within the printing area. These findings support the conclusions from above in that the printing laser can be focused inside the LC ink for a large set of different directors.

In our setup, we employ a half-wave plate on a motorized rotation mount to rotate the initial linear polarization of the printing laser perpendicular to the director. To obtain azimuthal polarization, we use a variable spiral waveplate that can be controlled via an external voltage. Depending on the voltage, it either allows to convert a certain linear polarization to an azimuthal polarization or leave the linear polarization as it is.

2.3. Exemplary Architectures

To prove that the presented method allows to control the director of the LCN during printing, we printed two different test structures with different director orientations. Both test structures consist of thin circular membranes supported by a cylindrical post. In the first case, the membrane is parallel to the substrate. In the second case, the membrane is perpendicular to the substrate. For both test structures, we varied the director in 45° steps within the plane of the membrane and also show directors perpendicular to the membranes. To estimate the projection of the optic axis (director) on the plane of the membrane, we employed a polarizing optical microscope (POM). In the POM, the test structure is located between two crossed polarizers, and the light transmitted through this configuration is detected. Whenever the projection of the test structure's optic axis is parallel or perpendicular to one of the polarizers, the polarization of the light is not altered by the test structure. Therefore, no light is transmitted in this case.

Optical bright-field images of the structures are depicted in **Figure 3** together with the intended director. It appears that the circular membranes deformed during the development step to an ellipsoidal shape with the long half axis along the intended director. The shrinkage is about 13% perpendicular to the director and close to zero along the director. Scanning electron microscopy (SEM) images of the structures are depicted in the same figure. Apart from the anisotropic shrinkage, no significant deviations from the targeted design are apparent. Additionally, POM images for two different configurations of the polarizers are depicted. The orientation of the polarizers is indicated on the left-hand side of the figure. Within small deviations, the POM images are black whenever a polarizer is parallel or perpendicular to the intended director. We attribute the small deviations from this behavior in the case of $\theta = 45°$ to director rotations due to (semi-) soft deformations[57] of the structures that result from strains due to shrinkage. We conclude that the director of the 3D printed test structures coincides with the intended director to within reasonable accuracy for many different director configurations. Furthermore, we conclude from the printing quality that the laser is well focused and that we especially do not have a double focus.

Up to now, we have only presented LCN structures with a single director orientation. However, it is also possible to print structures containing a spatial variation of the director orientation. To explore this possibility, we printed a structure that consists of a cylindrical post with eight bi-layered beams along the radial direction attached to it. The top view of the structure is depicted in **Figure 4**a together with the targeted spatial director distribution. The director within the beams is tangential to the beam on one side and perpendicular to the substrate on the other side. Since LCNs expand perpendicular to the director and shrink parallel to the director on heating, we expect a significant bending motion of the beams upon increasing the temperature.

Figure 4c shows an SEM image of the printed structure. Due to the anisotropic shrinkage during the development, the beams are already bent at room temperature. When increasing the sample temperature, the anticipated bending motion is clearly visible in Figure 4b and Movie S1, Supporting

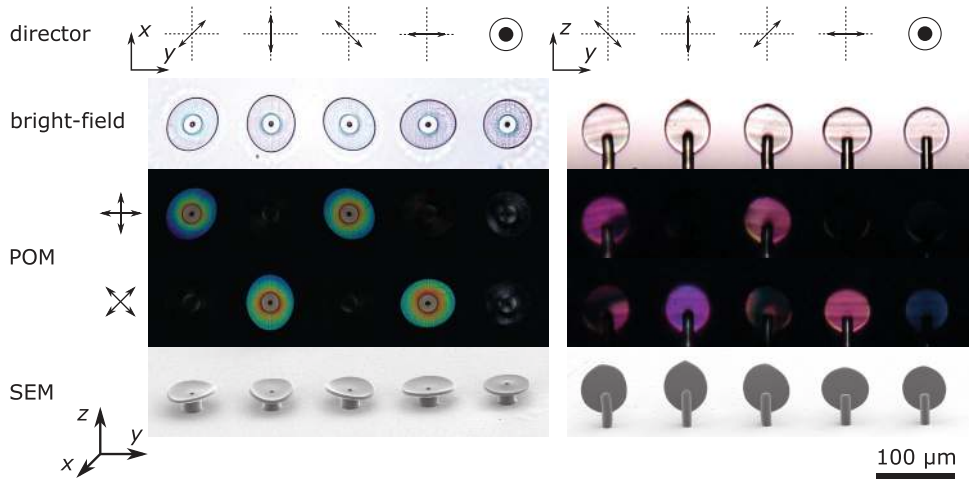

Figure 3. Circular membranes in the *x*-*y* plane and the *y*-*z* plane supported by cylindrical posts. The director varies as indicated in the top panel. In the second panel bright-field light microscope images of the structures are shown. The structures deformed during development and appear elliptical with their large axis along the intended director. The third and the fourth panel show POM images of the structures for two different orientations of the polarizers as indicated. The structures appear black whenever the intended director is parallel or perpendicular to a polarizer. The bottom panel shows SEM images of the structures. The defined shape of the structures indicates a good focus quality.

Information. There, bright-field images of the structure inside a heating stage are depicted for different temperatures. Since the direction of the bending motion is as expected, we conclude that the 3D printed spatial director distribution is as intended, too. However, the behavior versus temperature in Figure 4 is clearly continuous over a broad temperature range. This evidences that the manufactured LCN does not exhibit a sharp phase-transition temperature. Figure S6, Supporting Information, further quantifies this behavior. A recent paper assigns the smeared-out LCN phase-transition behavior to strong $\pi-\pi$ bonds in the LCN.[58]

The successful alignment of the director in the bi-layered beams has motivated us to explore yet more complex director distributions. In the following example, we considered a structure exhibiting a phase transition based on a thermally-induced mechanical buckling instability. We emphasize that this transition temperature is not directly connected to the LCN phase-transition temperature but is rather due to a designed

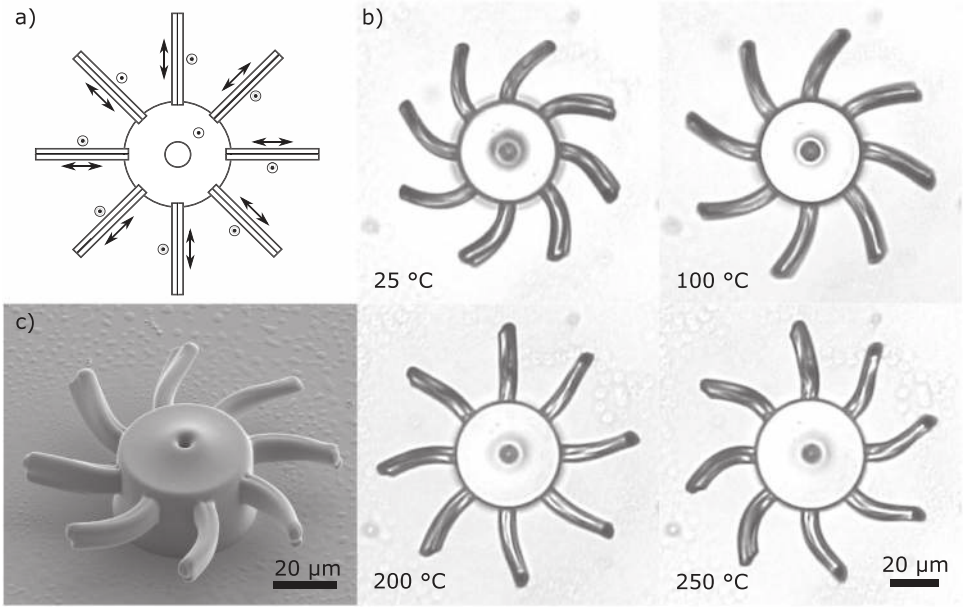

Figure 4. a) Schematic representation (top view) of the targeted structure. It consists of a cylindrical post attached to the substrate and eight bi-layered radial beams connected to the post. Arrows indicate the spatial director distribution. b) Bright-field light microscope images of the structure within a heating stage at four different temperatures. The beams are already bent at room temperature due to anisotropic shrinkage. With increasing temperature, the beams bend in the opposite direction. Movie S1, Supporting Information, shows the motion of the arms. c) SEM image of the 4D printed structure.

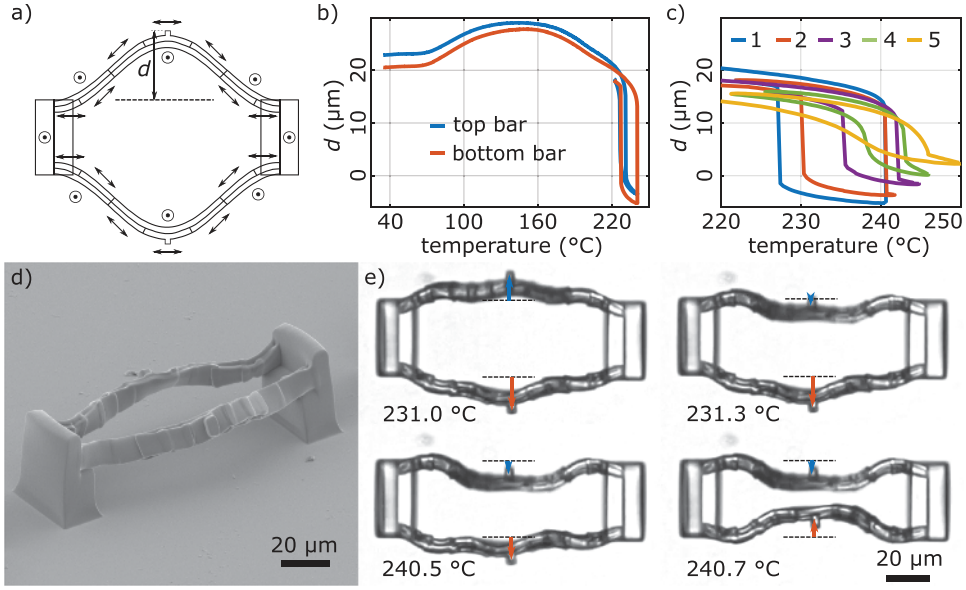

Figure 5. a) Schematic representation (top view) of the targeted structure. It consists of two cosine-shaped beams supported by two rectangular posts attached to the substrate. To track the motion of the beams, a small marker is attached to the middle of each beam. The motion is described in terms of *d* which is the distance between the marker and the line that connects the corners of the supporting posts, which is indicated by the dashed line. The arrows indicate the targeted spatial director distribution. b) The temperature is cycled from room temperature to 240 °C and back to 220 °C. *d* is plotted versus temperature and shows a sudden drop upon heating and sudden recovery upon cooling. A hysteresis behavior is obvious. c) We cycled the temperature several times to investigate the hysteresis behavior. A degradation of the structure is visible. d) A SEM image of the structure at room temperature. e) Bright-field light microscope images of the structure within a heating stage at four different temperatures. The temperatures are slightly above and slightly below the sudden drop in *d*. *d* is indicated by the blue and orange arrows. A mechanical buckling instability is visible for both bars. Movie S2, Supporting Information, shows the motion in real time.

mechanical instability. For such a structure, we expect a discontinuous mechanical motion at a specific critical temperature. Conceptually, such behavior allows to obtain macroscopic actuation when increasing the temperature by an infinitesimally small amount. The structure depicted in **Figure 5** consists of two rectangular-shaped posts that support two cosine-shaped bars. This design has been inspired by the work of Frenzel et al.[59] The director distribution within the bar is depicted in the top view of the structure in Figure 5a.

The structure is designed such that the bars straighten upon heating and therefore get compressed in between the two supporting posts. At some point, this configuration becomes unstable. Therefore, the bars relax in a sudden motion to the opposite side. To track the motion of the bars, they have a tip attached at the middle. The distance *d* of the tip to the line connecting the two attachment points of the respective bar is marked in Figure 5a. A SEM image of a printed sample is shown in Figure 5d. Again, deformations and distortions due to the anisotropic shrinkage of the material during the development are apparent.

To investigate whether the printed structure really shows the expected mechanical buckling instability, we heated the structure from room temperature to 240 °C and cooled it down again. During this cycle, we recorded optical bright-field images at different temperatures and tracked the tips of the respective bars and the outer corners of the posts via image cross-correlation.[60] From these data, we calculated the distance *d*, which is plotted for both bars versus temperature in Figure 5b.

In the heating step, we observed a continuous increase of *d* by about 6 µm for the top bar up to a temperature of about 140 °C. It was followed by a decrease of about 14 µm up to a critical temperature of 230 °C. Upon further increase of the temperature, *d* dropped by about 14 µm within a temperature interval of less than 0.3 °C. In the cooling step, we observed a recovery of *d* at a critical temperature of 226 °C within a temperature range of below 0.3 °C. Due to the difference in the critical temperatures, we observed a hysteresis behavior. For the bottom bar, we observed a similar behavior. However, the hysteresis behavior was more pronounced. There, the critical temperature for heating was about 240 °C, while the critical temperature for cooling was roughly the same as for the upper bar. The microscope images in Figure 5e show the structure at the critical temperatures and 0.3 °C above. From these images, the sudden deformation of the bars is clearly visible. The sudden deformation is also shown in Movie S2, Supporting Information. We attribute the slightly different behavior of the upper and the lower bar to sample imperfections.

The observed hysteresis of the thermally-induced mechanical buckling instability may be inherent to the design but can also be brought about by viscoelastic effects. To further investigate this hysteretic behavior, we have cycled the temperature five times around the critical temperatures for heating and cooling and monitored the distance *d* versus temperature. The result is depicted in Figure 5c. The amplitude of the jump in *d* decreases with increasing cycle number. In the fourth and fifth cycle, discontinuous buckling motion is no longer observed. We attribute this behavior to a permanent deformation of the LCN due to the large strains induced by the temperature cycling. We also observed a deterioration upon temperature cycling for

the structures shown in Figure 3. The corresponding data are presented in Figure S6 and Movie S3, Supporting Information. Nevertheless, with the structure shown in Figure 5, we succeeded in 4D printing a structure with a complex distribution of the director orientation leading to a thermally-induced mechanical buckling instability and hence to large-amplitude actuation for a minimal temperature swing.

3. Conclusion

In conclusion, we have presented a new approach allowing to 3D print complex LCN architectures with conceptually arbitrary spatial distributions of the director orientation in three dimensions. We have shown how to realize sufficiently homogeneous quasi-static electric fields of arbitrary direction in situ during the printing process to align the local director of the LC ink. Furthermore, we have shown that by employing a suitable polarization of the printing laser for a given director orientation, a single well-confined laser focus is obtained under conditions of focusing femtosecond laser pulses using a high-numerical-aperture objective lens. The combination of a variable spiral waveplate and a pivotable half-wave plate allows to automatically switch the polarization of light during the printing process. The combination of director alignment by quasi-static electric fields and polarization control, which can be dynamically adjusted for each voxel during the 3D printing process, allows for the making of complex 3D architectures in which every voxel in three dimensions can have an almost arbitrary orientation of the liquid crystal director.

We have illustrated the capabilities of the approach by three groups of examples using inks that have previously been established. While all examples have successfully been realized, they also exhibit limitations due to the ink that have been encountered previously by many other authors.[15,42,61] These limitations include anisotropic shrinkage, the large temperatures necessary for actuation, and material degradation after temperature cycling.

We emphasize that, in contrast to previously reported techniques,[7,8,14–16,41,42,51] our approach does not rely on any surface-mediated alignment of the director and hence allows for arbitrary 3D spatial distribution of the director orientation within the printed 3D structures. Furthermore, our approach is not limited to cell heights of only a few tens of micrometers like previous approaches.[7,8,14–16,41,42,51] Our manufacturing approach opens the door to complex 3D stimulus-responsive microstructures such as, for example, metamaterials, operating under ambient conditions. For such applications, the LCN properties would need to be improved though. Specifically, lower LCN transition temperatures have been demonstrated, but not for multi-photon 3D laser printing. Furthermore, LCN deterioration upon multiple cycling at large temperatures and strains would need to be reduced or eliminated in future work.

4. Experimental Section

Fabrication of the Electrodes: The electrodes were fabricated in a cleanroom to prevent dust on the electrode before the ITO evaporation, which would lead to spikes in the ITO layer that can cause electrical breakdowns. To fabricate the electrodes, D263M coverslips with a size of 13 mm × 13 mm × 0.17 mm were first cleaned. Therefore, the glasses were ultrasonicated alternatingly in baths of deionized water with a detergent and a bath of pure deionized water at 60 °C. In the first bath, Deconex OP 146 (4 vol%) was employed, and in the second bath, a solution of Deconex OP 12PA-x (2 vol%), and in the last bath a solution of Deconex OP 171 (2 vol%) were employed. The procedure was adapted from a procedure provided by Schott. After completing this procedure, the glasses were dried in a stream of N_2 gas. The cleaned glasses were coated on both sides with ITO by electron beam deposition at a rate of 0.5 Å s^{-1} with a distance of 39 cm between the crucible and the glasses at a partial O_2 gas pressure of $5{\cdot}10^{-5}$ Torr. Afterward, the glasses were heated to 550 °C for 1 h to oxidize the layer. Thereafter, the oven was switched off and the samples cooled down slowly in the oven to room temperature.

To structure the electrode, the ITO coverslips were spin-coated with a 3 µm thick layer of AZ10XT from Microchemicals at 4000 U min^{-1} on one side and pre-baked at 110 °C for 2 min in an oven. Afterwards, the coverslips were flood-illuminated with the frontside pattern for 29 s at an intensity of 13 mJ cm^{-2} by using a mask aligner (Karl Suess MA/BA 6). The other side of the coverslip was spin-coated with the same resist to protect it and pre-baked. The resist was developed in a mixture of AZ400K in deionized water at the ratio of 1:4 for 8 min. The ITO was etched with diluted aqua regia consisting of HCl (20 vol%) and HNO3 (5 vol%) for 30 min. Afterward, the resist was washed away with acetone in an ultrasonic bath. Then the above steps were repeated to structure the backside pattern. To isolate the electrode, a 100 nm thick layer of SiO_2 was evaporated via electron beam evaporation on both sides at a rate of 1 Å s^{-1} and a partial O_2 gas pressure of $1{\cdot}10^{-5}$ Torr.

To contact the electrode, a conductive epoxy glue (Polytec EC201) was used to fix a copper wire at the contact pads of the electrode. The electrode was fixed to its holder with a 30 µm thick polyimide tape. The copper wires fixed at the electrode pads were soldered to a copper conducting path on the holder.

Alignment of the Electrode: Due to the large extension of the electrode and the substrate compared to its distance, they must be closely parallel. To achieve this parallelism, an HeNe laser beam was reflected on the front lens of the objective lens before the immersion oil was added . The reflex was observed on a screen at a distance of about 60 cm. In the following, the electrode and the substrate were aligned such that all the reflexes fell on the same spot. Thereby an accuracy in parallelism of about 0.4 mrad was achieved.

To align the height of the electrode, an additional lens was added in a drop-in mount in front of camera to image the plane offset 100 µm below the nominal focal plane of the objective lens. The electrode was at the correct height if the camera image of the top pattern was sharp in the camera image.

To align the electrode central above the objective lens, four alignment markers were added to the top pattern of the electrode. Those are visible as squares in Figure 1a.

Substrates: The counter electrode consists of a sapphire piece of 5 mm × 5 mm × 0.43 mm, which was cut from a 2" c-plane, double side polished wafer (SITUS Technicals GmbH). Sapphire substrates were chosen due to their large electric permittivity compared to glass. This resulted in a lower voltage drop over the substrate for vertical electric fields. Instead of coating every substrate with ITO, the substrates were attached with a 30 µm thick polyimide adhesive tape on a glass substrate coated with ITO. In terms of electrostatics, this is equivalent, but more efficient in handling.

The substrates were functionalized with 3-(trimethoxysilyl)propyl methacrylate. First, the surface of the substrates was activated with an air plasma for 5 min. Subsequently, the substrates were placed inside a desiccator with a droplet of about 10 µL of silane for 1 h.

Ink Formulation: For the ink, 1,4-bis[4-(3- acryloyloxypropyloxy) benzoyloxy]-2-methylbenzene (16.5 wt%), 4-methoxybenzoic acid 4-(6-acryloyloxy-hexyloxy)phenyl ester (33.1 wt%), Irgacure 369 (0.7 wt%) and E7 (49.7 wt%) were mixed in a small vial and the mixture was heated to 80 °C under constant stirring. Afterward, the mixture was filtered

with a 0.45 µm PTFE syringe filter with a diameter of 13 mm to remove the monomer that did not solve in the E7. Prior to each printing job, the mixture was heated again to a temperature of 80 °C to ensure all monomer was dissolved. The reactive mesogens and the E7 mixture were bought from SYNTHON Chemicals GmbH & Co. KG. The composition of the ink is also depicted in Figure S1, Supporting Information.

Sample Development: To develop the sample, it was immersed in isopropanol at 40 °C for 90 s.[42] Afterward the sample was dried by evaporating the remaining isopropanol at ambient conditions.

Finite Element Method Simulation: The finite element method simulations were performed with the COMSOL Multiphysics electrostatics module. The geometry was implemented as depicted in Figure 1d and the permittivities of the different materials were set to $\varepsilon^{LC} = 19$, $\varepsilon^{electrode} = 4.6$, $\varepsilon_{\parallel}^{substrate} = 11.54$, $\varepsilon_{\perp}^{substrate} = 9.34$. It was assumed that the LC ink aligned to the electric field at any point. Under these conditions, it was sufficient to assume a single permittivity for the ink. The permittivity was assumed to be that of E7 along the direction of its dipole moment. At the electrode positions, the potentials given above were set as boundary conditions to the solver.

Electronic Setup: To set the potentials, a computer-controlled function generator was employed to generate a sinusoidal signal at 800 Hz with variable amplitude between 0 and 10 V. The signal was amplified by a factor of 300 using a HiVolt HA51U-3B2 amplifier.

Six variable voltage dividers were attached in parallel to the amplifier. A circuit diagram and a photograph are shown in Figure S4, Supporting Information. Each divider consists of a fixed capacitor of 50 pF (V5) or 33.3 pF (V1–V4, V6) and a variable capacitor ranging from 6 pF to 130 pF from Amidon. The variable capacitors were adjusted via computer-controlled stepping motors. The potential at each output was monitored via a fixed capacitive voltage divider consisting of a 1 pF and a 1 nF capacitor. The outputs of the variable voltage dividers were connected to the electrode via self-made coaxial cables of 40 cm length and a diameter of 2 cm. Those cables couple each pad to the ground with a capacity of approximately 15 pF. To prevent breakdowns due to a voltage between the objective lens and the pad with potential V5, the objective lens was put to the same electrical potential via a wire inside the electrode holder. The holder also isolated the objective lens from the optical table.

Since the capacitive coupling between the electrode pads V1–V5 with the substrate (V6) was on the order of 1 pF, it was necessary to model the six voltage dividers as a coupled system. A detailed description of the algorithm to set a desired set of voltages is given in the Supporting Information.

Optical Simulations: For the optical simulations, an ordinary refractive index of the LC ink was assumed to be 1.5 and the extraordinary index to be 1.7. The refractive indices of the electrode and the immersion oil were also chosen to be 1.5. The ITO layer was neglected . For the objective lens, a magnification of 25 and a numerical aperture of 0.8 were assumed. This results in an entrance pupil with a radius of 5.3 mm. The distance of the focal point of the objective lens and the interface between electrode and LC ink was chosen to be 100 µm. For the printing laser a collimated beam was assumed with a Gaussian intensity profile. The intensity dropped to e^{-2} at a radius of 4.75 mm.

Optical Setup: The overall 3D microprinting setup was described in full detail elsewhere.[62] A broadband half-wave plate was added in a motorized rotation mount followed by a variable spiral plate from Arcoptix at a conjugate plane of the entrance pupil of the objective lens. The half-wave plate was used to rotate the linear polarization of the printing laser perpendicular to the director. The spiral wave plate could be controlled by an external voltage such that the linear polarization was either kept or it was changed to an azimuthal polarization.

A Zeiss LCI Plan-Neofluar 25×/0.8 objective lens was employed with the correction ring set to oil. A scheme of the setup is depicted in Figure S5, Supporting Information.

Printing Parameters: In the following, all reported laser powers were measured at the entrance pupil of the objective lens. The power inside the laser focus was smaller due to losses in the objective lens and at the electrode. The employed laser was a Spectra Physics Mai Tai HP with a repetition rate of 80 MHz and a pulse width at the laser output of 90 fs. The center wavelength was chosen to be 790 nm. All samples were printed using galvanometric scanning.

The samples on the left-hand side of Figure 3 were printed in a spiral with a hatching of 0.08 µm and a slicing distance of 0.5 µm at a speed of 5 mm s^{-1}. The laser power was 28 mW for $\theta = 0°$ and 32 mW for $\theta = 90°$.

The samples on the right-hand side of Figure 3 were printed with straight hatching lines with a distance of 0.05 µm. The slicing distance was 0.5 µm and the scan speed was 5 mm s^{-1}. The laser power was 36 mW for $\theta < 90°$ and 24 mW for $\theta = 90°$.

For the sample shown in Figure 4, the post was printed in a spiral with a hatching of 0.08 µm and a slicing distance of 0.5 µm at a scan speed of 5 mm s^{-1}. The laser power was 46 mW. The bars attached to the post were printed with straight hatching lines along the bar with a distance of 0.2 µm and a slicing distance of 0.5 µm. The scan speed was 100 mm s^{-1} with a laser power of 101 mW for $\theta = 0°$ and 61 mW for $\theta = 90°$ and $\phi = 0°$, 62 mW for $\phi = \pm 45°$ and 63 mW for $\phi = 90°$.

For the sample shown in Figure 5, the two posts were printed with straight hatching lines spaced by 0.2 µm and a slicing distance of 0.5 µm at a scan speed of 100 mm s^{-1}. The laser power was 108 mW. The bars attached to the posts were printed with cosine-shaped hatching lines along the bar with a distance of 0.2 µm and a slicing distance of 0.5 µm. The scan speed was 100 mm s^{-1} with a laser power of 108 mW for $\theta = 0°$ and 67 mW for $\theta = 90°$ and $\phi = 0°$, 68 mW for $\phi = \pm 45°$ and 69 mW for $\phi = 90°$.

For all samples, the authors waited 20 ms after a stage movement in the z-direction of 0.5 µm and 2 s for stage movements in the z-direction larger than that to allow the director to re-align to the electric field after flow-induced misalignments.

The electric field strength was always chosen to be 0.3 V μm^{-1}.

Heating Stage: To heat the samples to 250 °C, an Instec mk2000 heating stage mounted in a microscope was employed. The heating in all experiments was done with a rate of 10 °C min^{-1}.

Supporting Information

Supporting Information is available from the Wiley Online Library or from the author.

Acknowledgements

This research was funded by the Deutsche Forschungsgemeinschaft (DFG, German Research Foundation) under Germany's Excellence Strategy via the Excellence Cluster 3D Matter Made to Order (EXC-2082/1-390761711), by the Carl Zeiss Foundation through the "Carl-Zeiss-Focus@HEiKA," by the Helmholtz program "Materials Systems Engineering" (MSE), by the Karlsruhe School of Optics & Photonics (KSOP), by the Max Planck School of Photonics (MPSP), and by the KIT Nanostructure Service Laboratory (NSL). This work was financed by the Ministry of Science, Research and the Arts of Baden-Württemberg as part of the sustainability financing of the projects of the Excellence Initiative II.

Open access funding enabled and organized by Projekt DEAL.

Conflict of Interest

The authors declare no conflict of interest.

Data Availability Statement

The data that support the findings of this study are openly available in the KITopen repository at https://doi.org/10.5445/IR/1000136888.

Keywords

3D two-photon lithography, 4D printing, electric field, liquid crystal network

Received: August 20, 2021
Published online:

[1] X. Kuang, D. J. Roach, J. Wu, C. M. Hamel, Z. Ding, T. Wang, M. L. Dunn, H. J. Qi, *Adv. Funct. Mater.* **2019**, *29*, 1805290.
[2] J. del Barrio, C. Sánchez-Somolinos, *Adv. Opt. Mater.* **2019**, *7*, 1900598.
[3] C. M. González-Henríquez, M. A. Sarabia-Vallejos, J. Rodriguez-Hernandez, *Prog. Polym. Sci.* **2019**, *94*, 57.
[4] C. A. Spiegel, M. Hippler, A. Münchinger, M. Bastmeyer, C. Barner-Kowollik, M. Wegener, E. Blasco, *Adv. Funct. Mater.* **2020**, *30*, 1907615.
[5] S. Joshi, K. Rawat, K. C., V. Rajamohan, A. T. Mathew, K. Koziol, V. Kumar Thakur, B. A.s.s, *Appl. Mater. Today* **2020**, *18*, 100490.
[6] Z. Xiong, M.-L. Zheng, X.-Z. Dong, W.-Q. Chen, F. Jin, Z.-S. Zhao, X.-M. Duan, *Soft Matter* **2011**, *7*, 10353.
[7] D. Martella, S. Nocentini, D. Nuzhdin, C. Parmeggiani, D. S. Wiersma, *Adv. Mater.* **2017**, *29*, 1704047.
[8] H. Zeng, P. Wasylczyk, C. Parmeggiani, D. Martella, M. Burresi, D. S. Wiersma, *Adv. Mater.* **2015**, *27*, 3883.
[9] C. Peters, O. Ergeneman, P. D. W. García, M. Müller, S. Pané, B. J. Nelson, C. Hierold, *Adv. Funct. Mater.* **2014**, *24*, 5269.
[10] C. Peters, M. Hoop, S. Pané, B. J. Nelson, C. Hierold, *Adv. Mater.* **2016**, *28*, 533.
[11] U. Bozuyuk, O. Yasa, I. C. Yasa, H. Ceylan, S. Kizilel, M. Sitti, *ACS Nano* **2018**, *12*, 9617.
[12] G. W. Milton, O. Mattei, *Proc. R. Soc., Ser. A* **2017**, *473*, 20160819.
[13] S. Xu, C. Wu, *Phys. Rev. Lett.* **2018**, *120*, 096401.
[14] S. Nocentini, F. Riboli, M. Burresi, D. Martella, C. Parmeggiani, D. S. Wiersma, *ACS Photonics* **2018**, *5*, 3222.
[15] S. Woska, A. Münchinger, D. Beutel, E. Blasco, E. Blasco, J. Hessenauer, O. Karayel, P. Rietz, S. Pfleging, R. Oberle, C. Rockstuhl, C. Rockstuhl, M. Wegener, M. Wegener, H. Kalt, *Opt. Mater. Express* **2020**, *10*, 2928.
[16] E. Sungur, L. Mager, A. Boeglin, M.-H. Li, P. Keller, K. D. Dorkenoo, *Appl. Phys. A* **2009**, *98*, 119.
[17] W. Zhang, H. Wang, H. Wang, J. Y. E. Chan, H. Liu, B. Zhang, Y.-F. Zhang, K. Agarwal, X. Yang, A. S. Ranganath, H. Y. Low, Q. Ge, J. K. W. Yang, *Nat. Commun.* **2021**, *12*, 112.
[18] L. D. Zarzar, P. Kim, M. Kolle, C. J. Brinker, J. Aizenberg, B. Kaehr, *Angew. Chem.* **2011**, *123*, 9528.
[19] M. Hippler, E. Blasco, J. Qu, M. Tanaka, C. Barner-Kowollik, M. Wegener, M. Bastmeyer, *Nat. Commun.* **2019**, *10*, 232.
[20] D. Jin, Q. Chen, T.-Y. Huang, J. Huang, L. Zhang, H. Duan, *Mater. Today* **2020**, *32*, 19.
[21] T. Watanabe, M. Akiyama, K. Totani, S. M. Kuebler, F. Stellacci, W. Wenseleers, K. Braun, S. R. Marder, J. W. Perry, *Adv. Funct. Mater.* **2002**, *12*, 611.
[22] Z. Xiong, X.-Z. Dong, W.-Q. Chen, X.-M. Duan, *Appl. Phys. A* **2008**, *93*, 447.
[23] A. Tudor, C. Delaney, H. Zhang, A. J. Thompson, V. F. Curto, G.-Z. Yang, M. J. Higgins, D. Diamond, L. Florea, *Mater. Today* **2018**, *21*, 807.
[24] M. R. Lee, I. Y. Phang, Y. Cui, Y. H. Lee, X. Y. Ling, *Small* **2015**, *11*, 740.
[25] B. Kaehr, J. B. Shear, *Proc. Natl. Acad. Sci. USA* **2008**, *105*, 8850.
[26] E. Descrovi, F. Pirani, V. P. Rajamanickam, S. Licheri, C. Liberale, *J. Mater. Chem. C* **2018**, *6*, 10428.
[27] I. Roppolo, A. Chiappone, A. Angelini, S. Stassi, F. Frascella, C. F. Pirri, C. Ricciardi, E. Descrovi, *Mater. Horiz.* **2017**, *4*, 396.
[28] H. A. Houck, E. Blasco, F. E. Du Prez, C. Barner-Kowollik, *J. Am. Chem. Soc.* **2019**, *141*, 12329.
[29] H. Cui, R. Hensleigh, D. Yao, D. Maurya, P. Kumar, M. G. Kang, S. Priya, X. (Rayne) Zheng, *Nat. Mater.* **2019**, *18*, 234.
[30] T. J. White, D. J. Broer, *Nat. Mater.* **2015**, *14*, 1087.
[31] Z. He, G. Tan, D. Chanda, S.-T. Wu, *Opt. Express* **2019**, *27*, 11472.
[32] M. O. Saed, A. Gablier, E. M. Terentjev, *Chem. Rev.* **2021**, https://doi.org/10.1021/acs.chemrev.0c01057.
[33] L. Tan, A. C. Davis, D. J. Cappelleri, *Adv. Funct. Mater.* **2021**, *31*, 2007125.
[34] M. del Pozo, C. Delaney, C. W. M. Bastiaansen, D. Diamond, A. P. H. J. Schenning, L. Florea, *ACS Nano* **2020**, *14*, 9832.
[35] M. E. McConney, A. Martinez, V. P. Tondiglia, K. M. Lee, D. Langley, I. I. Smalyukh, T. J. White, *Adv. Mater.* **2013**, *25*, 5880.
[36] L. T. de Haan, V. Gimenez-Pinto, A. Konya, T.-S. Nguyen, J. M. N. Verjans, C. Sánchez-Somolinos, J. V. Selinger, R. L. B. Selinger, D. J. Broer, A. P. H. J. Schenning, *Adv. Funct. Mater.* **2014**, *24*, 1251.
[37] T. H. Ware, M. E. McConney, J. J. Wie, V. P. Tondiglia, T. J. White, *Science* **2015**, *347*, 982.
[38] B. A. Kowalski, V. P. Tondiglia, T. Guin, T. J. White, *Soft Matter* **2017**, *13*, 4335.
[39] J.-H. Kim, M. Yoneya, H. Yokoyama, *Nature* **2002**, *420*, 159.
[40] Y. Xia, G. Cedillo-Servin, R. D. Kamien, S. Yang, *Adv. Mater.* **2016**, *28*, 9637.
[41] H. Zeng, P. Wasylczyk, G. Cerretti, D. Martella, C. Parmeggiani, D. S. Wiersma, *Appl. Phys. Lett.* **2015**, *106*, 111902.
[42] Y. Guo, H. Shahsavan, M. Sitti, *Adv. Mater.* **2020**, *32*, 2002753.
[43] C. P. Ambulo, J. J. Burroughs, J. M. Boothby, H. Kim, M. R. Shankar, T. H. Ware, *ACS Appl. Mater. Interfaces* **2017**, *9*, 37332.
[44] A. Kotikian, R. L. Truby, J. W. Boley, T. J. White, J. A. Lewis, *Adv. Mater.* **2018**, *30*, 1706164.
[45] M. López-Valdeolivas, D. Liu, D. J. Broer, C. Sánchez-Somolinos, *Macromol. Rapid Commun.* **2018**, *39*, 1700710.
[46] D. J. Roach, X. Kuang, C. Yuan, K. Chen, H. J. Qi, *Smart Mater. Struct.* **2018**, *27*, 125011.
[47] M. O. Saed, C. P. Ambulo, H. Kim, R. De, V. Raval, K. Searles, D. A. Siddiqui, J. M. O. Cue, M. C. Stefan, M. R. Shankar, T. H. Ware, *Adv. Funct. Mater.* **2019**, *29*, 1806412.
[48] A. Kotikian, C. McMahan, E. C. Davidson, J. M. Muhammad, R. D. Weeks, C. Daraio, J. A. Lewis, *Sci. Robot.* **2019**, *4*, eaax7044.
[49] E. C. Davidson, A. Kotikian, S. Li, J. Aizenberg, J. A. Lewis, *Adv. Mater.* **2020**, *32*, 1905682.
[50] A. Kotikian, J. M. Morales, A. Lu, J. Mueller, Z. S. Davidson, J. W. Boley, J. A. Lewis, *Adv. Mater.* **2021**, *33*, 2101814.
[51] C. C. Tartan, P. S. Salter, T. D. Wilkinson, M. J. Booth, S. M. Morris, S. J. Elston, *RSC Adv.* **2017**, *7*, 507.
[52] Y.-C. Cheng, H.-C. Lu, X. Lee, H. Zeng, A. Priimagi, *Adv. Mater.* **2020**, *32*, 1906233.
[53] I. Dierking, *J. Phys. D: Appl. Phys.* **2001**, *34*, 806.
[54] B. Richards, E. Wolf, D. Gabor, *Proc. R. Soc. Lond. Ser. Math. Phys. Sci.* **1959**, *253*, 358.
[55] M. C. Simon, L. I. Perez, *J. Mod. Opt.* **1991**, *38*, 503.
[56] P. Yeh, *Surf. Sci.* **1980**, *96*, 41.
[57] M. Warner, E. M. Terentjev, *Liquid Crystal Elastomers*, OUP, Oxford **2007**.
[58] J. M. McCracken, B. R. Donovan, K. M. Lynch, T. J. White, *Adv. Funct. Mater.* **2021**, *31*, 2100564.
[59] T. Frenzel, C. Findeisen, M. Kadic, P. Gumbsch, M. Wegener, *Adv. Mater.* **2016**, *28*, 5865.
[60] T. Frenzel, J. Köpfler, A. Naber, M. Wegener, *Sci. Rep.* **2021**, *11*, 2304.
[61] S. Nocentini, D. Martella, C. Parmeggiani, D. S. Wiersma, *Materials* **2016**, *9*, 525.
[62] V. Hahn, P. Kiefer, T. Frenzel, J. Qu, E. Blasco, C. Barner-Kowollik, M. Wegener, *Adv. Funct. Mater.* **2020**, *30*, 1907795.